Millimeter-wave and Terahertz Devices

Academic and Research Staff
Professor Qing Hu

Graduate Students
Hans Callebaut, Erik Duerr, Kostas Konistis, Sushil Kumar, Juan Montoya, Ben Williams

Introduction

Millimeter-wave and THz frequencies (f = 0.1-10 THz) remain one of the most underdeveloped frequency ranges, even though the potential applications in remote sensing and imaging, spectroscopy, and communications are great. This is because the millimeter-wave and THz frequency range falls between two other frequency ranges in which conventional semiconductor devices are usually operated. One is the microwave frequency range, and the other is the near-infrared and optical frequency range. Semiconductor devices which utilize the classical diffusive transport of electrons, such as diodes and transistors, have a high frequency limit. This limit is set by the transient time and parasitic RC time constants. Currently, electron mobility and the smallest feature size which can be fabricated by lithography limit the frequency range to below several hundred GHz. Semiconductor devices based on quantum mechanical interband transitions, however, are limited to frequencies higher than those corresponding to the semiconductor energy gap, which is higher than 10 THz for most bulk semiconductors. Therefore, a large gap exists from 100 GHz to 10 THz in which very few devices are available.

Semiconductor quantum-effect devices (which can be loosely termed "artificial atoms"), including both vertically grown quantum-well structures and laterally confined mesoscopic devices, are human-made quantum mechanical systems in which the energy levels can be chosen by changing the sizes of the devices. Typically, the frequency corresponding to the intersubband transitions is in the millimeter-wave range ($\Delta E \sim$ 1-4 meV) for the lateral quantum-effective devices, and THz to infrared for the vertical quantum wells. It is therefore appealing to develop ultrahigh-frequency devices, such as THz lasers utilizing the intersubband transitions in these devices.

In our group, we are systematically investigating physical and engineering issues that are relevant to devices operating from millimeter-wave to THz frequencies. Specifically, we are working on THz lasers based on intersubband transitions in quantum wells, ultrahigh-frequency heterostructure bipolar transistors based on phonon-enhanced forward diffusion, and on-chip terahertz spectrometers using ultrafast photoconductive switches.

Terahertz Lasers Based on Intersubband Transitions

Project Staff
Ben Williams, Hans Callebaut, Sushil Kumar, and Qing Hu, in collaboration with Dr. John Reno at Sandia National Lab.

Semiconductor quantum wells are human-made quantum mechanical systems in which the energy levels can be designed and engineered to be of any value. Consequently, unipolar lasers based on intersubband transitions (electrons that make lasing transitions between subband levels within the conduction band) were proposed for long-wavelength sources as early as the 1970s. However, because of the great challenge in epitaxial material growth and the unfavorable fast nonradiative relaxation rate, unipolar intersubband-transition lasers (also called quantum-cascade lasers) at mid-infrared wavelengths were developed only recently at Bell Laboratories. This achievement is remarkable, but the technique used in the original quantum-cascade lasers will not be directly applicable for the longer-wavelength THz range because of two major obstacles. First, the energy levels corresponding to THz frequencies (1 THz = 4 meV) are quite narrow, so the requirements for the design and fabrication of suitable quantum wells are demanding. Because of the narrow separation between subband levels, heating and electron-electron scattering will have a much greater effect. Also, the small energy scales of THz photons make the detection and analysis of spontaneous emission (a crucial step toward developing lasers) quite difficult. Second, mode confinement, which is essential for any laser oscillation, is difficult at longer wavelengths. Conventional dielectric-waveguide confinement is not applicable because the evanescent field penetration, which is proportional to the wavelength and is on the order of several tens of microns, is much greater than the active gain medium of several microns. Currently, we are investigating to overcome these two obstacles in order to develop intersubband-transition lasers. We have made good success in generating and detecting THz emission signals and on developing a novel mode confinement method using metallic waveguide structures. Key results are summarized in the following sections.

THz emitters using electron-LO-phonon scattering for depopulation

Following the design principle of the original QCLs, we have designed intersubband THz emitters based on a three-level system. The top two subband levels, E_3 and E_2, form the radiative pair, while the ground state E_1 is at $\geq \hbar\omega_{LO}$ below E_2. Since it is energetically allowed, the fast electron-LO-phonon $E_2 \ E_1$ scattering will help to keep the population in E_2 low, and therefore maintain a population inversion between E_3 and E_2. However, because E_3-$E_2 < E_2$-$E_1 \geq \hbar\omega_{LO}$ for THz emitters, it is difficult to implement this three-level system based on an intrawell transition scheme, in which both E_3 and E_2 are primarily located in a single well. The bottom of this well would have to be raised relative to the rest of the structure so that E_2-$E_1 \geq \hbar\omega_{LO}$. Raising the bottom of the well would require adding aluminum to the well material GaAs, which would cause a significant alloying scattering and result in a broad emission linewidth.

Our design of the three-level systems is based on a scheme that the radiative transition takes place in a coupled double-well structure. A third well, which is much wider than the two wells, contains the ground-state level E_1. In our earlier designs, the wavefunctions of E_3 and E_2 are primarily localized in separate wells, thus the $E_3 \rightarrow E_2$ transition is spatially diagonal. This design offers the advantage of a high selectivity in injection into E_3 and removal from E_2, because of the spatial separation of the two wavefunctions. However, the diagonal nature of the radiative transition is quite sensitive to scattering due to interface roughness and alloy in the barrier, and thus the emission showed rather broad spectra ($\Delta f \sim$ 3-5 THz).

It is well known that in a coupled double-well structure, the wavefunctions of the two lowest levels are spatially extended with a strong overlap at the anticrossing. Because of this spatial overlap, both levels are subject to the same interface and alloy scattering, and thus the emission linewidth of radiative transition between the two levels is reduced. In an improved structure, whose band structure and wavefunctions are shown in Fig. 1, we have taken advantage of this feature to enhance the strength of the radiative $E_3 \rightarrow E_2$ transition. In the structure shown in Fig. 1, the core is a three-well module of GaAs/Al$_{0.3}$Ga$_{0.7}$As heterostructures (inside the dashed box), with three barriers B$_1$ (4.5 nm), B$_2$ (2.8 nm), B$_3$ (5.6 nm) and

three wells W_1 (8.8 nm), W_2 (5.9 nm), and W_3 (6.8 nm). The collector barrier B_1 is center δ-doped at a level of $6\times10^{10}/cm^2$ in order to provide dynamic charges. Under the designed bias of 51 mV per module, the ground state E_1' (not shown) of a previous module is aligned with E_3. Thus, the upper level E_3 can be selectively populated via resonant tunneling. At this bias, the energy separation $E_{32} \approx 11$ meV (corresponding to 2.67 THz), and the dipole moment $z_{32} \approx 30$ Å. The energy separation $E_{21} \approx 40$ meV $\geq \hbar\omega_{LO}$, enabling electron-LO-phonon $E_2 \rightarrow E_1$ scattering for depopulation.
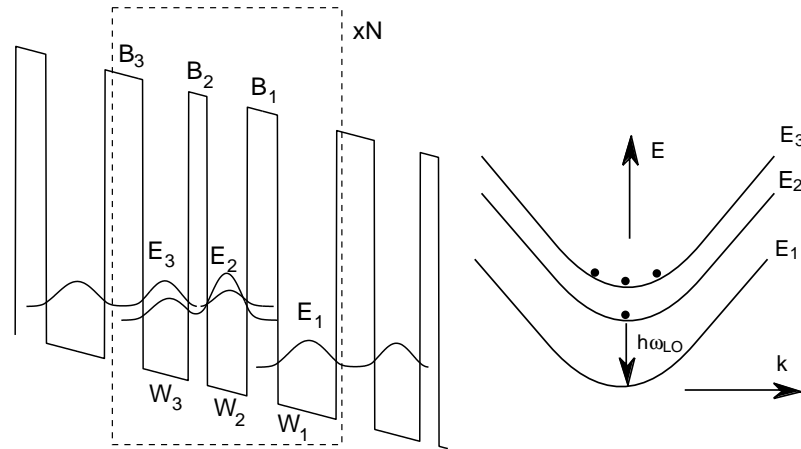

Figure 1. Schematic of a three-level system based on a triple quantum-well structure shown inside the dashed box. On the right is the dispersion relation between the energy and the transverse momentum.

In order to measure the intersubband THz emission and resolve its spectra, we constructed a set-up that included a Fourier transform infrared spectrometer (FTIR) with a composite Si bolometer as its detector. The system's schematic is shown in Fig. 2. We have improved this system and perfected our measurement techniques so that THz emission measurements can be routinely performed on our emitters with output power levels of 1-10 pW.
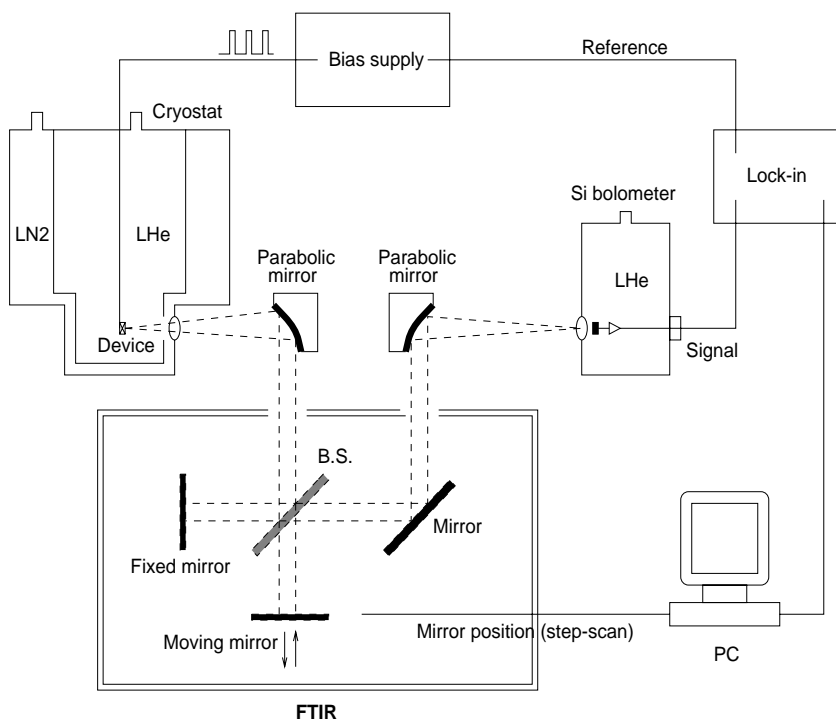
Figure 2.   Far-infrared measurement set-up that uses a Fourier transform spectrometer to spectrally resolve the emitted THz signals.

Our emission spectra reveal a clear peak due to the $E_3 \rightarrow E_2$ intersubband emission. A representative spectrum taken at 5-K device temperature is shown in Fig. 3(a), which was taken at the designed bias of 1.6 V (~30×51 mV). The measured peak frequency of 2.57 THz (10.6 meV) is close to the designed value of 11.3 meV. The FWHM linewidth is as narrow as 0.47 THz (1.9 meV). In order to verify the intersubband origin of the measured emission spectra, we have measured emission spectrum at a high bias of 4.0 V at which the energy levels are severely misaligned. The spectrum is shown in the inset of Fig. 3(a), and it bears little resemblance to the main figure.

Spectra were also taken with the cold stage cooled with liquid nitrogen to 80 K. One taken at a bias of 1.6 V is shown in Fig. 3(b). The main peak is essentially the same as the one measured at 5 K, with a slightly broader linewidth of 0.52 THz (2.14 meV). The linewidth measured at 80 K is expected to be similar to that at 5 K, since nonparabolicity is negligible for THz intersubband emitters. Nevertheless, our experimental verification is encouraging for the development of intersubband THz sources at elevated temperatures.
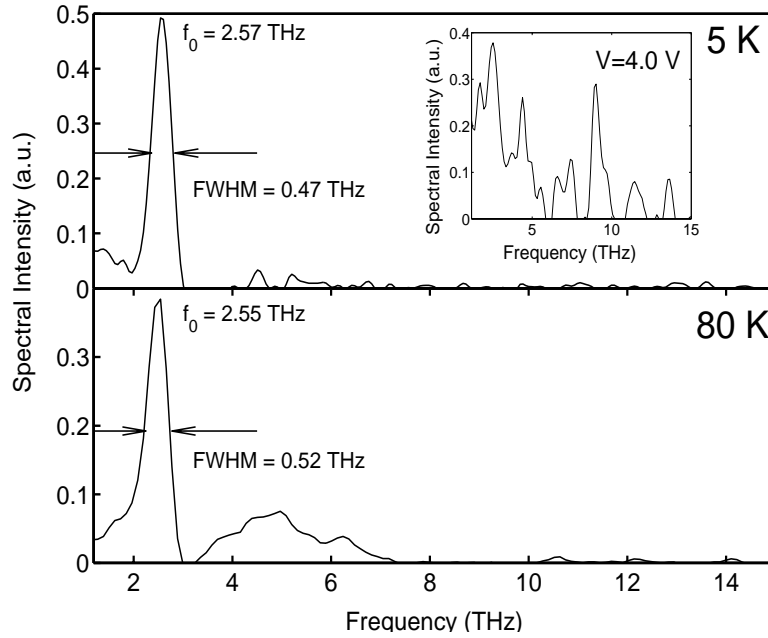
Figure 3. Spectrally resolved THz intersubband spontaneous emission taken at (a) 5-K and (b) 80-K bath temperature under 1.6-V bias. The inset shows the spectrum for 4.0-V bias, clear evidence that emission results from intersubband transitions.

Role of interface and confined phonon modes

Just like the electronic wavefunctions forming discrete subbands in MQW structures, phonon spectra also become discrete, forming spatially localized interface and confined modes. Despite this parallel analogy, bulk LO-phonon mode has been used to calculate the scattering times in QCLs. This practice may be justified for mid-infrared QC lasers, in which $E_3-E_2 >> \hbar\omega_{LO}$, so that the sum-rule yields the same result as obtained from using the bulk mode. However, as Dutta and Stroscio recently pointed out, such a practice may be questionable for THz intersubband lasers, because $E_3-E_2 < \hbar\omega_{LO}$ and $E_2-E_1 \approx \hbar\omega_{LO}$.

We have investigated the role of the complex phonon spectra on the intersubband scattering rates. In the model used in our calculations, the phonon modes are described by the potential $\phi(\mathbf{r})$ resulting from the polarization field created by atomic displacements in a polar semiconductor. Each material layer of index i is described by a dielectric function $\varepsilon_i(\omega)$ as given by the Lyddane-Sachs-Teller relations, which vanishes at the LO-phonon frequencies. For lattice vibrations, since there are no free charges, the phonon potential must satisfy $\varepsilon(\omega - \nabla^2\phi(\mathbf{r})) = 0$. Two types of solutions exist: interface modes for which $\nabla^2\phi(\mathbf{r}) = 0$, and confined modes for which $\varepsilon(\omega = 0$.

For the confined modes, $\varepsilon(\omega = 0$ and therefore $\omega = \omega_{LO}$, where ω_{LO} is the bulk LO-phonon frequency in the layer of interest. Since ω_{LO} changes at the heterointerfaces, the potential must vanish there, and $\phi(\rho)$ can be described in terms of sine wave modes in z. For the interface modes, $\varepsilon(\omega) \neq 0$, and the modes have frequencies $\omega \neq \omega_{LO}$. The potential solution is a linear combination of exponential terms peaked at the interfaces, hence the name of "interface mode". For our GaAs/AlGaAs quantum-well structures, there are usually two "GaAs-like" and one "AlAs-like" modes associated with each GaAs/AlGaAs interface. Thus, for the six interfaces in our triple-well structures shown in Fig. 1, there are a total 18 interface modes. The total scattering rate is the sum of the contributions from these 18 interface modes and all the confined

modes (30 lowest modes were used in our calculations with the contributions from the higher modes negligible).

We used the transfer matrix approach to account for the electromagnetic boundary conditions and obtain the mode potentials and dispersion relations for the interface modes. As it turns out, the 12 "GaAs-like" modes are clustered around 33-36 meV, close to the bulk GaAs LO-phonon energy. The 6 "AlAs-like" modes are clustered around 45-47 meV, close to the bulk AlAs LO-phonon energy. Special care was taken to ensure a proper normalization of each mode, which was verified by limiting cases. The dispersion relation and the phonon potential profiles for the interface modes are shown in Fig. 4.
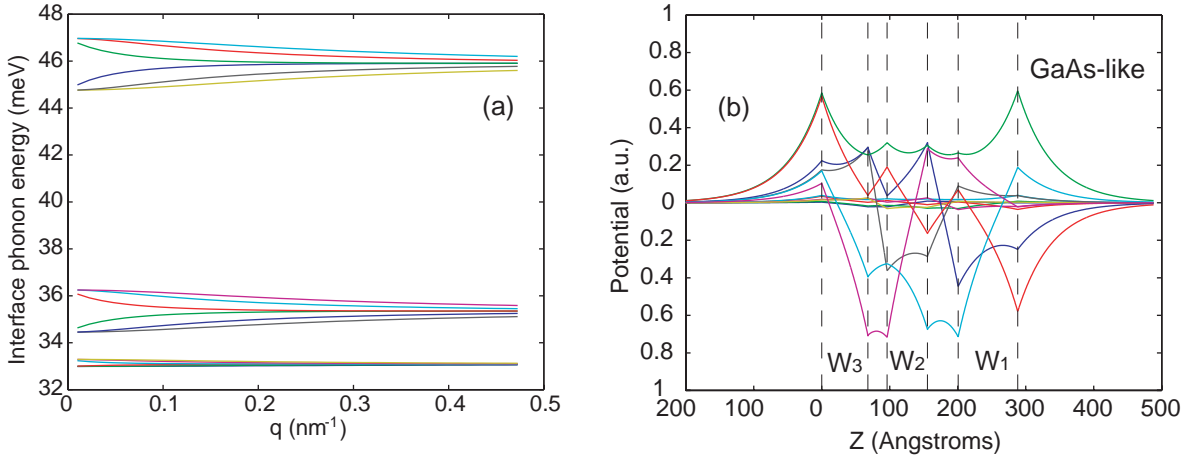

Figure 4.   (a) Dispersion relation of all the 18 interface modes; (b) phonon potential profiles of the 12 "GaAs-like" interface modes associated with our triple quantum-well device.

In order to address the key issue of the optimum subband separation E_{21}, we have calculated the maximum total scattering rate as a function of E_{21}, as shown in Fig. 5. The rate shows two peaks, one at ~35 meV due to the "GaAs-like" modes and the other at ~47 meV due to the "AlAs-like" modes. As a comparison, we also include the scattering rate calculated using the bulk GaAs LO-phonon mode. It is clear that the scattering rate is ~30% lower than the bulk mode if E_{21} ~ 36 meV, because of the exclusion of the "AlAs-like" modes. However, increasing E_{21} to ~47 meV does not increase the total scattering rate appreciably. This is because that at E_{21} ~ 47 meV, even though all the phonon modes participate in the scattering, the rapid decrease in the strength of the "GaAs-like" modes away from their resonance (at ~36 meV) diminishes most of the benefit gained from including more active phonon modes.
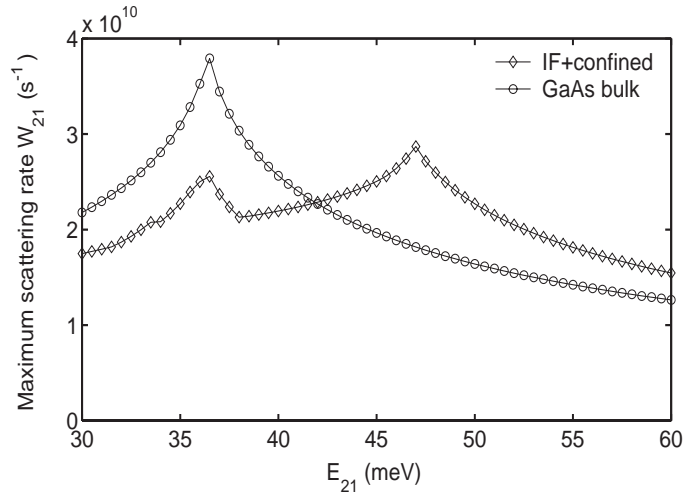
Figure 5. Maximum scattering rate versus subband separation E_{21} for the three-level structure shown in Fig. 1. Maximum scattering rate calculated with GaAs bulk modes is present for comparison.

In Fig. 6, we plot the key figure of merit $\tau_3(1 - \tau_{21}/\tau_{32})$, which is proportional to the population inversion Δn_{32}, as a function of the scattering time τ_{32}. As E_{21} increases from 36 to 47 meV, the increase in Δn_{32} is marginal at a given τ_{32}. Even this marginal increase should be taken with a grain of salt. As E_{21} increases from 36 to 47 meV, there will be an additional 11 meV energy dissipation per electron. This extra energy dissipation will further raise the electronic temperature. As a result, τ_{32} decreases because of LO-phonon scattering of hot electrons. Fig. 6 shows that a reduction in τ_{32} could undo any advantage gained by increasing E_{21} to 47 meV. The conclusion from our analysis is that in electrically pumped THz intersubband emitters, because the barriers are thin and Al concentrations are low (x ≤ 0.3), the contribution from the higher-energy "AlAs-like" modes only barely make up for the loss in the strength of "GaAs-like" modes. Thus, increasing E_{21} from 36 to 47 meV will only yield at the best a marginal (if any at all) improvement in population inversion Δn_{32}.
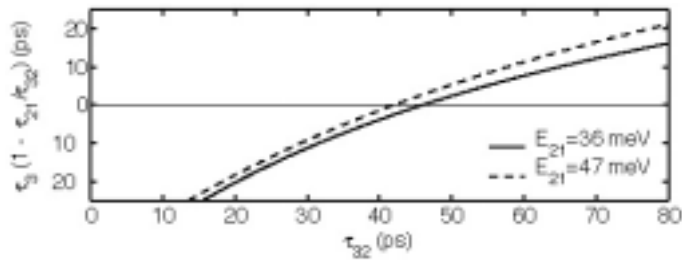

Figure 6. Plot of the quantity $\tau_3(1-\tau_{21}/\tau_{32})$, which is proportional to the population inversion Δn_{32}, versus the lifetime τ_{32} for the structure shown in Fig. 1.

Intrawell THz emitters using resonant tunneling for depopulation

Fig. 7(a) shows the calculated band diagram of another type of THz intersubband emission structure that we investigated recently. In this structure, the radiative transition takes place between two subband levels primarily located in one quantum well. We consider this scheme as "intrawell" as opposed to the interwell scheme discussed earlier. It is known that the intrawell scheme yields a larger dipole moment and a narrower emission linewidth, because the subband separation is less sensitive to impurity and interface roughness scattering.
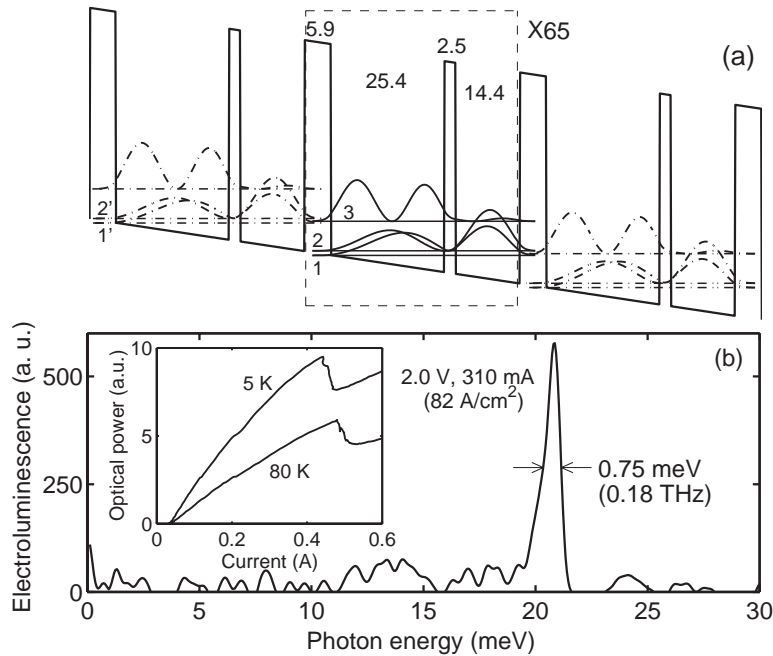

Figure 7. (a) Computed conduction band profile and squared magnitude wavefunctions for the intrawell device. (b) Electroluminescence spectrum at 5 K for an applied bias of 2.0 V. The inset displays the emitted power versus current.

The core of the structure shown in Fig. 7(a) is a coupled double-well module shown inside the dashed box. Sixty-five nominally identical modules are cascade connected. Under the designed bias of ~20 mV/module, the lower level E_2 in the wide well is aligned with the lowest level E_1 in the narrow well, which in turn is aligned with the upper level in the wide well of the following module. The radiative transition takes place between E_3 and E_2, which have a strong spatial overlap as can be seen in Fig. 7(a). The depopulation of E_2 is facilitated through "resonant tunneling" from E_2 to E_1, which deserves special attention and will be discussed in the following. The calculated dipole moment $z_{32} \approx 6.0$ nm at the designed bias, as a result of the strong radiative coupling in this intrawell scheme.

Fig. 7(b) shows a measured emission spectrum taken at a bias of 2.0 V, which is somewhat greater than the designed bias (65×20 mV ≈ 1.3 V). The spectrum shows a clear peak at 21 meV (~5.04 THz), with a FWHM linewidth as narrow as 0.75 meV (0.18 THz). The measured emission frequency is close to the calculated subband separation $E_{32} \approx 18.5$ meV, and the narrow linewidth indicates the high quality of the MBE growth.

The term "resonant tunneling" usually refers to electron transport between two subband levels close in energies. There has been a long debate on whether this process should be analyzed as intersubband

scattering between two spatially extended wavefunctions (the scenario of coherent resonant tunneling), or as tunneling between two spatially localized states (the scenario of incoherent sequential tunneling). This question is not merely academic, but is crucial for the successful development of intersubband THz lasers, as the two transport mechanisms yield very different depopulation rates. For coherent resonant tunneling, the electron transport is facilitated by fast (<1 ps) electron-electron intersubband scattering. For incoherent sequential tunneling, the depopulation rate is determined by the barrier transparency, which can be much slower than the first scenario.

In the coherent picture, the energy difference between any pair of two subbands has a finite minimum value, known as the anticrossing gap Δ, which characterizes how strongly the two subbands are coupled. In contrast, in the incoherent scenario, the two subband wavefunctions are spatially localized in different wells. Their energy levels can be degenerate and thus may be arbitrarily close at resonance. Based on the coherent model, we have calculated Δ_{21} = min $|E_2-E_1| \approx 2.5$ meV. Even though current-field (*I-B*) magneto-tunneling spectroscopy has been successfully used to resolved subband separations of ~20 meV, the resolution of the anticrossing gaps of only a few meV requires the measurement of conductance $G = dI/dV$ to enhance the energy resolution and sensitivity.

Fig. 8 shows both *I-B* and *G-B* curves measured in a voltage range near the E_2-E_1 anticrossing. The *I-B* curves show a single-period oscillation, revealing an energy separation of ~19 meV close to the calculated intersubband spacing. The *G-B* data show a closely separated double resonance, as highlighted by the double arrows. The dependence of these conductance peaks on bias is plotted in Fig. 8(c), and it displays a typical anticrossing behavior between a Stark shifted peak and another fixed at ~6.0 T (~21 meV). This 21-meV peak corresponds to 3→2 transition, which agrees with the emission data. The Stark shifted peak corresponds to 3→1 transition, as the two wavefunctions are spatially more separated than those of E_3 and E_2. The minimum separation of the two conductance peaks is ~1.7 meV, which is close to the calculated anticrossing gap of $\Delta_{21} \approx 2.5$ meV. The overall dependence of the conductance peaks on the bias agree reasonably well with the calculated energy differences E_{31} and E_{32}, as shown in Fig. 8(c). Our work shows that in the particular structure shown in Fig. 7(a), the $E_2 \to E_1$ depopulation should be modeled as intersubband scattering between two spatially extended states.
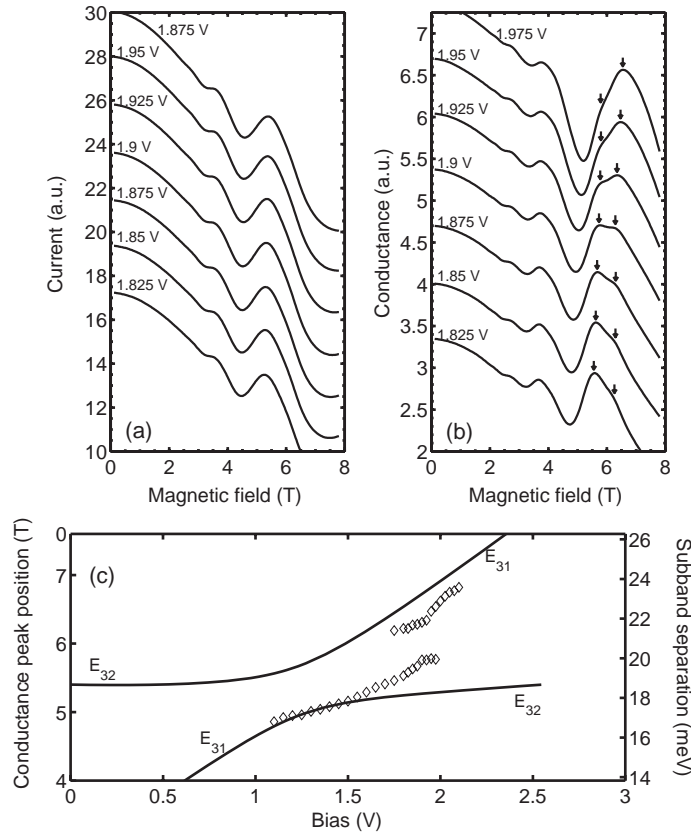
Figure 8. Current (a) and conductance (b) versus magnetic field for several biases. (c) Positions of the double peaks in *G-B* plots versus the bias. The solid lines are calculated subband energy separation E_{32} and E_{31}.

AlGaAs/GaAs HBT with enhanced forward diffusion

Sponsors
AFOSR
Grant F49620-00-1-0331

Project Staff
Kostas Konistis and Qing Hu, in collaboration with Prof. M. Melloch at Purdue University, and Prof. C. G. Fonstad.

One of the key limits of high-frequency operation of bipolar transistors is the base transient time, which is proportional to the square of the base width when the base transport is dominated by diffusion. Consequently, high-frequency bipolar transistors tend to use thin bases (<100 nm) that results in a short base transient time and a high cut-off frequency f_T. However, for high frequency operations, it is not the current gain that matters most. Rather, it is the unilateral power gain that determines the operating frequency of any three-terminal devices. The frequency f_{max}, at which the power gain is unity, is determined by both f_T and RC time constant. Because of the peculiar geometry of bipolar transistors, the electrical contact to the base is always made from the side. Thus, a thin base, which is important to yield a high f_T, will inevitably result in a high sheet resistance and a lowering of f_{max}. It is this difficult trade-off

between f_T and f_{max} that lead Prof. S. Luryi and his co-workers to propose a novel heterostructure bipolar transistor, whose band diagram is shown in Fig. 9.
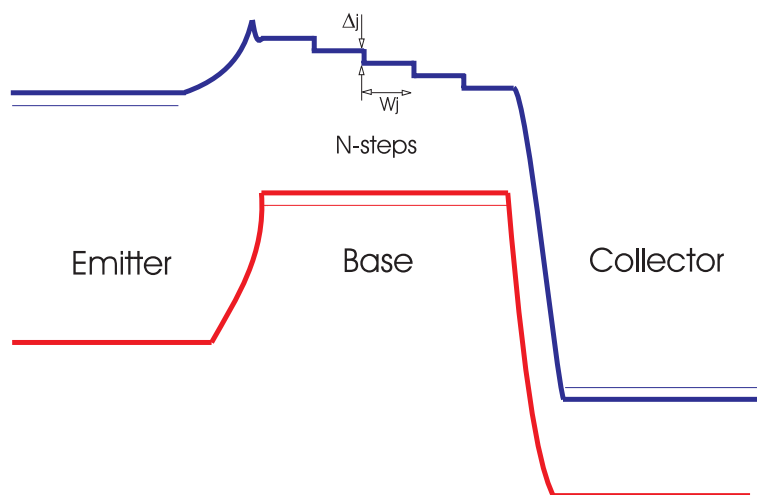

Figure 9.   Energy band diagram of an HBT with stepwise base. The energy drop Δ at each step is slightly greater than the LO-phonon energy (36 meV) in GaAs. Thus, electrons encounter very fast LO-phonon emission scattering (with a time ~0.1 ps) when they go over the edge of a step. Consequently, backward diffusion is significantly reduced and forward diffusion is enhanced.

The main feature of this novel HBT is that its base is graded like a staircase. The height of each step Δ is slightly greater than the LO-phonon energy in GaAs (36 meV). Thus, electrons will encounter very fast LO-phonon emission scattering (with a time ~0.1 ps) when they go over the edge of a step. Consequently, backward diffusion is significantly reduced. In a way, the edge of each step resembles and performs a similar function as the base-collector interface: any injected excess minority carrier will be quickly swept down the energy potential. As a result, each step acts like a minibase, as far as the diffusion transport is concerned. The resulting minority carrier concentration assumes a nearly periodic distribution, provided that the energy drop is greater than the sum of LO-phonon and thermal energy to ensure a fast scattering and prohibit backward diffusion. The total base transient time is therefore approximately N times the transient time of each step, whose width can be as narrow as 30 nm, yielding a high f_T. On the other hand, all the N steps are connected in parallel for the base contact, reducing the base resistance by an approximate factor of N. The combination of a thin effective base and small base resistance will yield a high f_{max}.

The use of LO-phonon scattering as a resetting mechanism introduces the concept of independent cascade of base transport factors. In our analysis, the intrinsic part is modeled by device physics whereas the extrinsic are treated as lumped circuit elements. A simple approach that captures most of the physics is to define the transport as the product of the individual base steps assuming perfect resetting LO mechanism. As a result, the total base transport factor is a simple product of the transport factor of each step, as shown in Fig. 10. It can be seen clearly, as the number of steps N increases, the amplitude of the base transport factor increases, resulting in a higher cut-off frequency.
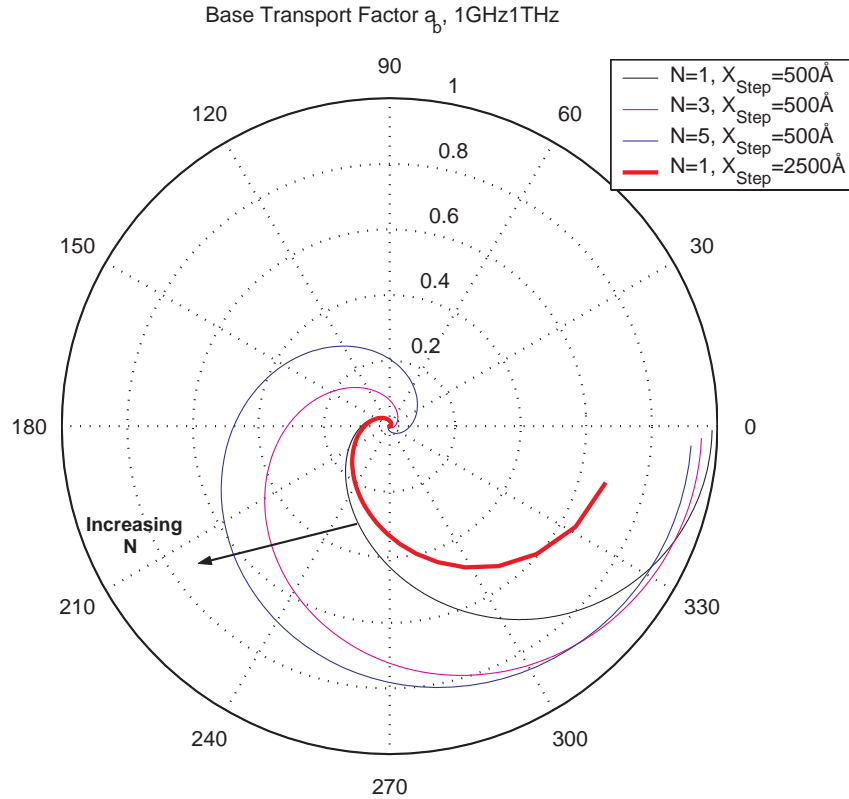
Base Transport Factor a_b, 1GHz1THz

Figure 10.   Polar plot of base transport factor in frequency, for N steps and XStep step size.

One interesting result of our analysis is the existence of resonances of the unilateral power gain. Their physical mechanism is closely linked with the current-phase delay. A base structure introduces both phase delay and magnitude attenuation of current. As the frequency of operation increases, the phase delay increases and at a certain frequency the voltage and current acquire opposite phases, which will yield a resonance if the amplitude attenuation is not too overwhelming. A short base offers small phase delay and resonance occurs at high frequencies where the magnitude attenuation is strong. On the other hand, a long base may provide a large phase delay but the heavy attenuation at low frequencies smoothes out the unilateral gain peaks. For a multi-step base, the total phase delay is the sum of each step, while the total attenuation is the product of each step, enhancing the possibilities of achieving resonance. As can be seen in Fig. 10, the base transport factor of multi-step base HBTs crosses the real axis with an appreciable amplitude, Fig. 11 shows both the current gain and unilateral power gain as a function of frequency for N =1-6. Clearly, even though f_T decreases somewhat as the number of steps N increases, f_{max} barely changes due to the reduced base resistance of high-N bases. Furthermore, resonance can be achieved above 100 GHz by using multi-step base HBTs, which is promising for the development of high-frequency fundamental oscillators.
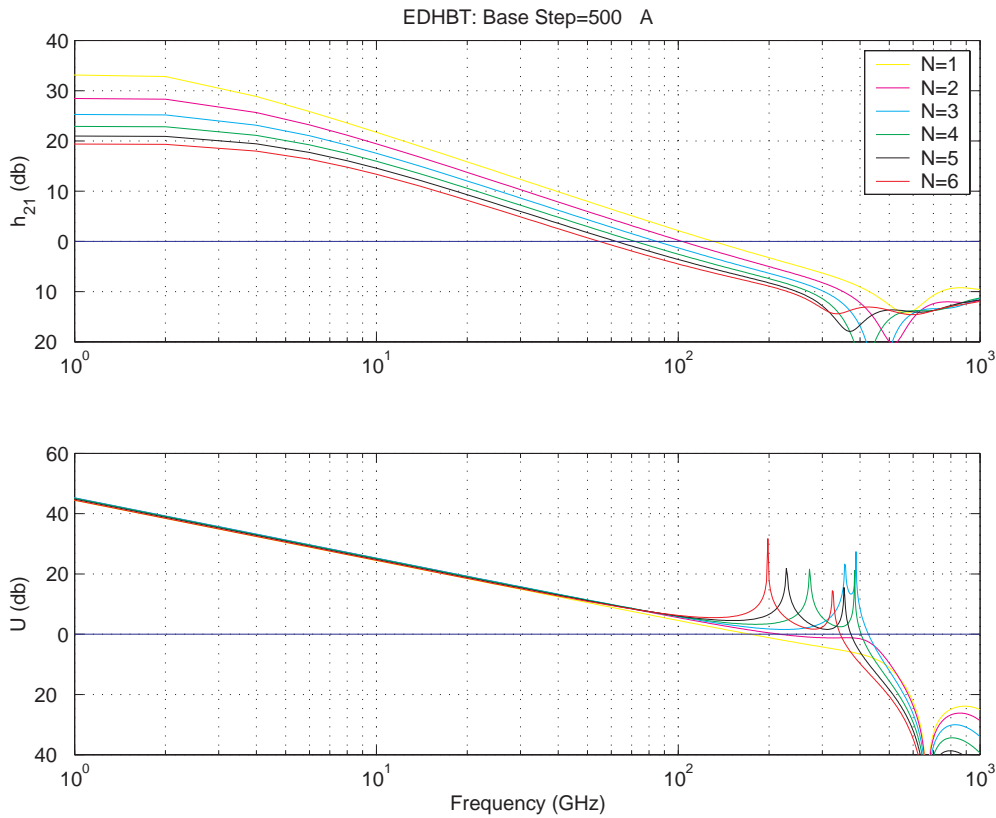
Figure 11.   Current gain h_{21} and Unilateral power gain U in frequency for X_{Step} =500 Å and variable number of steps. The resonance (peaks in U) is clearly shown above 100 GHz, which is promising for the development of high-frequency fundamental oscillators.

An on-chip frequency-domain submillimeter-wave spectrometer

Sponsor
Rosenblith Fellowship

Project Staff
Juan Montoya and Q. Hu

Because of the frequency limitation of semiconductor electronic devices, measurement instruments such as network analyzers can operate only below approximately 100 GHz. Thus, even if ultrahigh-frequency HBTs can be developed, they can only be directly measured up to 100 GHz, with higher-frequency performance extrapolated according to certain frequency roll-off models. Clearly, such an extrapolated measurement will not be applicable to measuring high-frequency resonance such as that shown in Fig. 11. It will be very useful to develop on-chip systems that can characterize device performance up to THz frequencies. A promising component for such systems is ultrafast photoconductive switches made of low-temperature-grown (LTG) GaAs materials. When pumped with two coherent laser beams, such switches can generate and detect photocurrent with a modulation frequency beyond one THz.

Furthermore, photoconductive emitters and receivers are attractive as components of sub-millimeter-wave spectroscopy systems because of their tunability, compactness and ability to be monolithically integrated with antennas, transmission lines and microelectronic devices. Such systems can be classified either as time-domain or frequency-domain systems. Time-domain systems, which contain a photoconductive pulse emitter and sampler excited by a mode-locked laser, are the most investigated. They have been used for free-space characterization of semiconductor materials, and on-chip characterization of ultrafast devices and circuits with 2.7 ps time resolution. The frequency resolution is the inverse of the time span over which the propagating pulse is sampled. This span is determined by the length of an optical delay line, which usually results in a frequency resolution broader than 1 GHz.

The emitter and receiver of a frequency-domain spectrometer will be pumped by two coherent cw laser beams with frequencies ω_1 and ω_2, instead of short laser pulses. If the response time is sufficiently fast, the emitter switch will generate an ac photocurrent with a frequency $|\omega_2-\omega_1|$, which can easily exceed 1 THz. Illuminated by the same two laser beams with a controlled delay, the receiver switch can be used to perform a homodyne detection of the ac photocurrent generated from the emitter. In combination with high-frequency transmission lines, they can form on-chip spectrometers with THz bandwidths. Fig. 12 illustrates a schematic of such a spectrometer that can be used to characterize common-emitter performance of high-frequency HBTs.
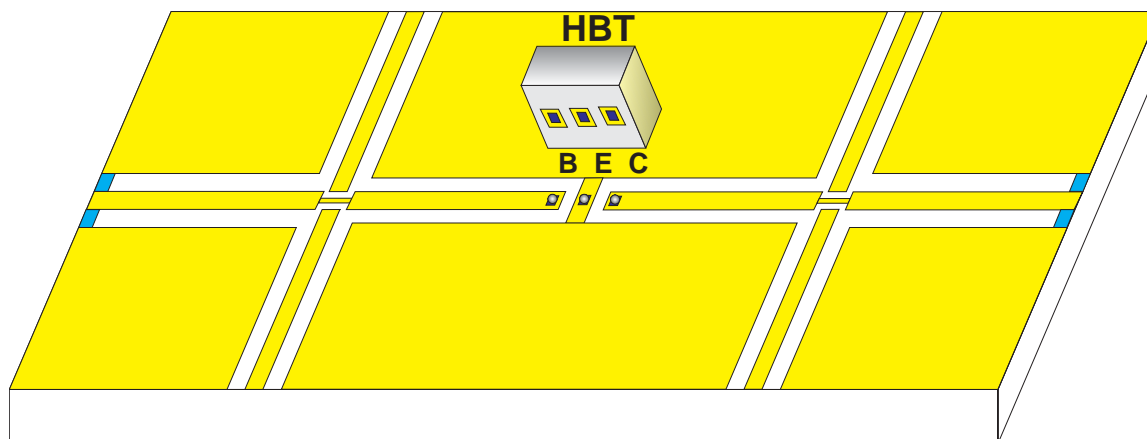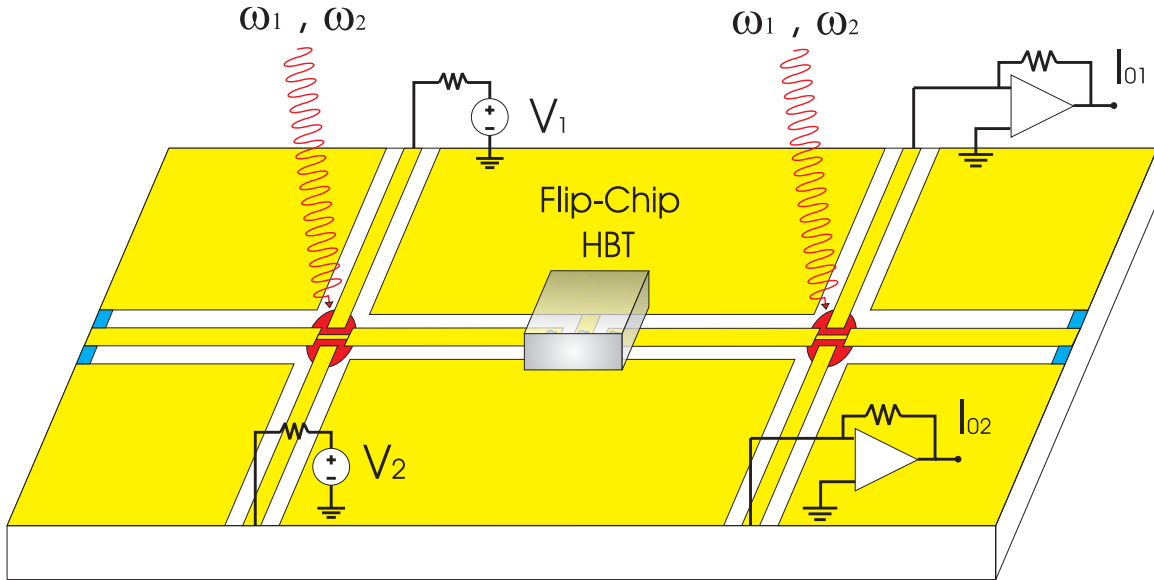
Figure 12.   Schematic of a on-chip spectrometer that uses ultrafast photoconductive switches to generate and detect ultrahigh-frequency signals.

Because of the broad bandwidth (>1 THz) and a high frequency resolution (better than 1 MHz), such a spectrometer is also adequate for molecular line spectroscopy. In combination with microchambers, the spectrometer can be part of a microfluidic, "lab on a chip"-type circuit, which can be used as on-chip sensors for chemical and biological agents. As the first step in the development of an on-chip frequency-domain spectrometer, we have investigated the performance of an on-chip transceiver containing only uninterrupted coplanar waveguides (CPWs).

Our circuit, shown in Fig. 13(a), has a biased pump photoconductor and an unbiased probe photoconductor connected by a main CPW, and other parasitic CPWs which provide DC electrical contact to the photoconductors. As illustrated in Fig. 13(a), we excited propagating electromagnetic waves at the pump by illuminating the pump photoconductor with two overlapping diode laser beams with a difference frequency f = $\omega_2 - \omega_1$. We performed homodyne detection of those waves by illuminating the probe with a delayed portion of the same laser beams. The relative delay between the pump and probe beams is the phase Φ. The output DC current I_{o1} should vary sinusoidally with Φ, $I_{o1}(\Phi) = I_o \cos(\Phi+\delta)$, because of the homodyne detection performed at the probe photoconductor. The argument of cosine contains two terms: the phase Φ, which is due only to the path lengths of the pump and probe beams; and the phase δ, which describes the response of the circuit and any device or specimen inserted in it. For example, δ may be non-zero because of the dispersion of the CPWs or circuit resonance. Our aim was to measure I_o and δ as functions of f. Together, I_o and δ contain all the information necessary for coherent spectroscopy.
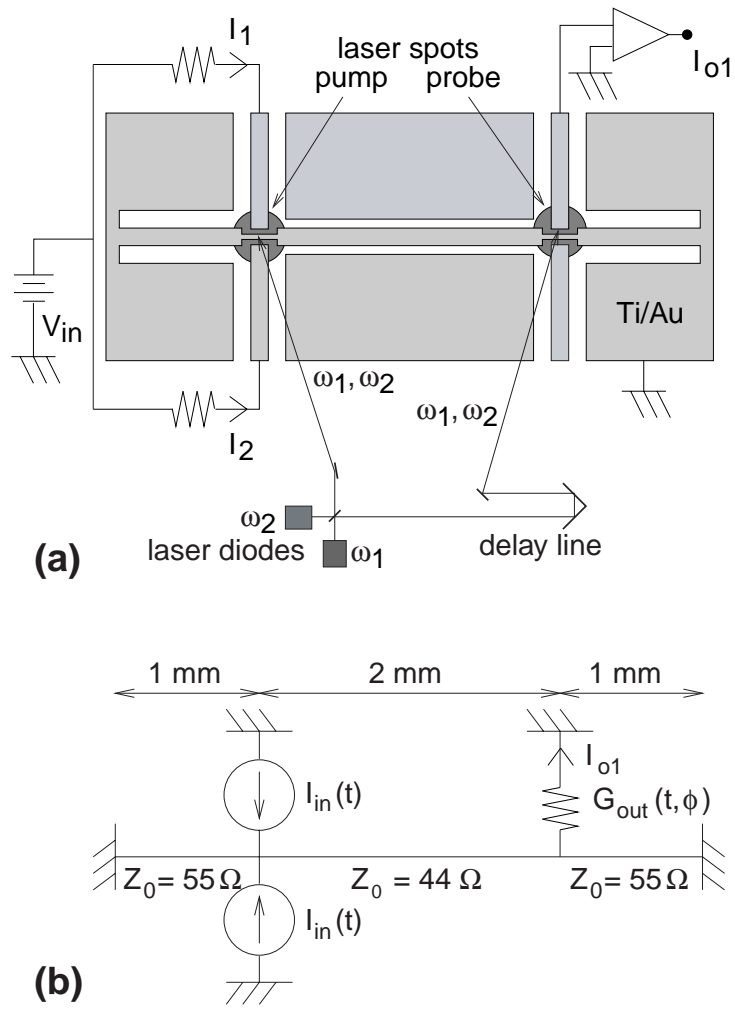
Figure 13.   (a): Diagram of the experimental circuit, showing its electrical bias and optical input. (b) Microwave circuit model of the experimental circuit.

We fit the measured spectra to a model based on the circuit shown in Fig. 13(b). The two active regions of the pump photoconductor are modeled as current sources. Similarly, the single utilized active region of the probe photoconductor is modeled as the time-varying conductance. We assume that the CPWs have a propagation constant $\Gamma = \alpha(f) + j2\pi f/v_p$, where $\alpha(f)$ is the attenuation constant to be fit to the data, and v_p is the phase velocity of a coplanar transmission line on a semi-infinite GaAs substrate. We use standard microwave circuit analysis to calculate I_{o1}, the Φ-dependent DC current generated at the probe.
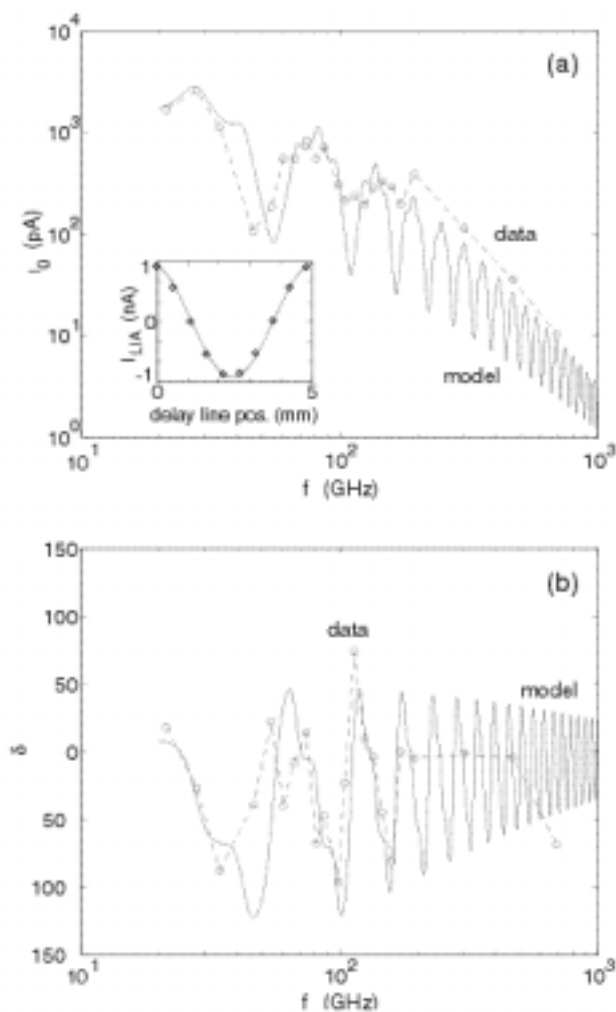
Figure 14.   Measured data and model of the amplitude and phase spectra (a) $I_o(f)$ and (b) $\delta(f)$. Inset: output of lock-in amplifier vs. delay line position at f=27.9 GHz, compared to a best-fit sinusoid.

Our model was fit to the data with reasonable fitting parameters. As shown in Fig. 14, the agreement between the model and the measured results is quite good, validating the microwave-circuit analysis of our on-chip submillimeter-wave transceiver.

Publications

1.   B. S. Williams and Q. Hu, "Optimized energy separation for phonon scattering in three-level terahertz intersubband lasers," J. Appl. Phys. **90**, 5504 (2001).

2.   K. Konistis and Q. Hu, "Numerical study of a GaAs-based heterojunction bipolar transistor with stepwise alloy-graded base," to be published in J. Appl. Phys. (2002).

3.   B. S. Williams, H. Callebaut, Q. Hu, and J. L. Reno, "Magnetotunneling spectroscopy of resonant anticrossing in THz intersubband emitters," Appl. Phys. Lett. **79**, 4444 (2001).

4.   H. Callebaut and Q. Hu, "Design analysis of interband-pumped intersubband THz lasers," submitted to Appl. Phys. Lett. (2001).

5.   Hu, Q., B. S. Williams, M. R. Melloch, and J. L. Reno, "Terahertz Emitters Based on Intersubband Transitions," to be published in Future Trend in Microelectronics: The Nano Millennium, S. Luryi, J. Xu, A. Zaslavsky, eds., John Wiley & Sons, New York, 2002.

Conference Presentations

1.   Hu, Q., "Terahertz Emitters Based on Intersubband Transitions," presented at Advanced Research Workshop on Future Trends in Microelectronics, Ile de Bendor, France, June (2001). (Invited)

2.   Hu, Q., "Electron-phonon scattering in THz emitters and electronics," presented at PHONONS 2001, Dartmouth College, Hanover, NH, August (2001). [Invited]

3.   B. S. Williams, H. Callebaut, Q. Hu, M. R. Melloch, J. L. Reno, "Terahertz intersubband emission in structures with and without LO-phonon assisted depopulation," presented at the 6th International Conference on Intersubband Transitions in Quantum Wells (ITQW'01), Monterey, CA, September (2001).

4.   H. Callebaut and Q. Hu, "Design of an interband-pumped THz intersubband laser," presented at the 6th International Conference on Intersubband Transitions in Quantum Wells (ITQW'01), Monterey, CA, September (2001).

5.   Q. Hu, "Terahertz Emission," ARO Quantum Cascade Lasers Workshop, Arlington, Virginia, October (2001). [Invited]

6.   Q. Hu, "Terahertz Emitters Based on Intersubband Transitions," 2002 Workshop on Frontiers in Electronics (WOFE'02), St. Croix, U. S. Virgin Island, January (2002). (Invited)

Theses

Master thesis

Hans Callebaut, thesis title, "GaAs/AlGaAs Far-Infrared Quantum Cascade Laser," August, 2001.